Wind and Structures, *Vol. 17, No. 6 (2013) 647-670*
DOI:http://dx.doi.org/10.12989/was.2013.17.6.647

Computational study of a small scale vertical axis wind turbine (VAWT): comparative performance of various turbulence models

Lazaros Aresti[1], Mustafa Tutar[*2,3], Yong Chen[1] and Rajnish K. Calay[4]

[1]*School of Engineering and Technology, University of Hertfordshire, Collage Lane Campus, Hatfield, Hertfordshire AL10 9AB, UK*
[2]*Mechanical and Manufacturing Department, MGEP, Mondragon Goi Eskola Politeknikoa, Loramendi 4 Apartado 23, 20500, Mondragon, Spain*
[3]*IKERBASQUE, Basque Foundation for Science, 48011,Bilbao, Spain*
[4]*Narvik University College, Lodve Langes Gate 2, 8505-Narvik, Norway*

(Received November 16, 2012, Revised July 15, 2013, Accepted July 30, 2013)

Abstract. The paper presents a numerical approach to study of fluid flow characteristics and to predict performance of wind turbines. The numerical model is based on Finite-volume method (FVM) discretization of unsteady Reynolds-averaged Navier- Stokes (URANS) equations. The movement of turbine blades is modeled using moving mesh technique. The turbulence is modeled using commonly used turbulence models: Renormalization Group (RNG) k-ε turbulence model and the standard k-ε and k-ω turbulence models. The model is validated with the experimental data over a large range of tip-speed to wind ratio (TSR) and blade pitch angles. In order to demonstrate the use of numerical method as a tool for designing wind turbines, two dimensional (2-D) and three-dimensional (3-D) simulations are carried out to study the flow through a small scale Darrieus type H-rotor Vertical Axis Wind Turbine (VAWT). The flows predictions are used to determine the performance of the turbine. The turbine consists of 3- symmetrical NACA0022 blades. A number of simulations are performed for a range of approaching angles and wind speeds. This numerical study highlights the concerns with the self-starting capabilities of the present VAWT turbine. However results also indicate that self-starting capabilities of the turbine can be increased when the mounted angle of attack of the blades is increased. The 2-D simulations using the presented model can successfully be used at preliminary stage of turbine design to compare performance of the turbine for different design and operating parameters, whereas 3-D studies are preferred for the final design.

Keywords: wind turbine; turbulence models; vertical axis wind turbine (VAWT); computational fluid dynamics (CFD)

1. Introduction

Renewable energy is fast becoming an affordable alternative to fossil fuel in the power generation sector. Various alternative systems i.e., wind turbines, photovoltaic systems and geothermal energy, have already started to power not only some houses but many cities around the world. The most efficient system developed for power generation so far is the wind turbine (Varol

∗Corresponding author, Professor, E-mail: mtutar@mondragon.edu

http://www.techno-press.org/?journal=was&subpage=8 ISSN: 1226-6116 (Print), 1598-6225 (Online)

2001). Wind energy can be converted to a maximum of fifty nine per cent of useful wind energy according to the Betz limit (Betz 1920).

Through time, different designs of wind turbines have been developed. There are two different types of wind turbines, Vertical and Horizontal axis wind turbines. The axis also states the direction that the turbine encounters the wind. The most commonly used so far is the horizontal axis wind turbine.

Horizontal axis wind turbines (HAWTs) are the conventional wind turbines that are mostly used with three blades. The main rotor shaft and the generator are on the top of the tower as well as the yawing mechanism that is required to face the wind direction in order to achieve an optimum power output.

All blades take advantage of the wind velocity due to the yawing mechanism which is achieved through a computer controlled motor. Modern horizontal axis wind turbines' blades can be remotely adjusted in matters of angle of attack to provide the optimum angle for maximum power output. The tower base also influences the output as the wind turbines can reach higher wind velocities in higher altitude and wind shear (Spera 1994). However, due to many moving parts horizontal wind turbines may require high maintenance.

Vertical axis wind turbines (VAWTs) are initially started as drag devices (Savonious 1931) and only recently researchers have given emphasis into the lift driven vertical axis wind turbines. They can take advantage of any wind direction where wind shifts direction or where turbulent flow exists. Vertical rotor does not require a yawing mechanism for accepting the wind from any direction so they need less moving parts and in addition it can provide direct rotary drive to a fixed load (Beri and Yao 2011). All other components (including mechanical and electrical components) that require maintenance are located at the ground level providing easier and faster access compromising reduced costs for maintenance (Hau 2006). The main drawback for the vertical axis wind turbines is the non-self-starting capability. Much research though-out the years has been conducted for an elucidation of the problem (Grylls *et al.* 1978, Drees *et al.* 1978) with recent use of cambered airfoils on a straight bladed Darrieus type vertical axis wind turbine (Beri and Yao 2011).

In addition, blades are subject to high dynamic loading due to the full crown rotation. The key drawbacks of a VAWT include difficulties for modeling the wind flow conditions accurately (due to the complex of its interfering blades region) and analysis of prototype prior to manufacturing. Therefore, realistic design models for analysis are critical. Further researches (Hwang *et al.* 2006 and El-Samanoudy *et al.* 2010) are also conducted in order to overcome the self-starting issue. The Cycloturbine has an end tail with the ability to change pitch angle. At low tip speed ratios the pitch angle changes to compromise the turbine from a lift driven device to a drag driven device in order to self-start and then the pitch angle changes back to its original position. However the initial pitching device is overall heavy and complex in use. Newer active control mechanisms have been designed recently in order to achieve improved efficiency over the fixed blade pitch angle (Seong *et al.* 2006).

Numerical and experimental studies have been conducted by various researchers to increase the capability of the VAWT. A recent innovative one compromises different design parameters; pitch angle, number of blades, airfoil type, turbine radius and its chord length, on the performance of a Giromill VAWT (El-Samanoudy *et al*. 2010). Through experimental data it has been proven that the above parameters have a significant impact on the performance output and an increase of the values, and result in higher C_p and C_t.

It is also found that cambered airfoils result in increasing the starting torque of low tip-speed ratio (TSR) and thereby eliminating the starting problems of the VAWT (Beri and Yao 2011).

The results have shown an increase of torque with self starting potential but a reduction in peak efficiency compared with symmetrical airfoils (Beri and Yao 2011, Kirke and Lazauskas 1991). There have been considerable efforts in combined experimental and computational studies of aerodynamics performance of VAWTs to transfer the wind's force directly to the rotor shaft, which is directly connected to a generator that converts the energy into electricity for their high efficient diversified applications.

The aim of the paper is to numerically investigate the dynamic torque output on a small scale Vertical axis Darrieus H-rotor wind turbine. The design consists of high solidity rotor, which results in high torque at low speeds. However, one disadvantage of Darrieus type VAWT is self-starting capabilities. Numerical simulations can be useful in investigating the effect of change in the mounted angle of attack on self-starting capabilities in order to optimize the position with respect to wind direction. Therefore, a suitable numerical approach to model and simulate aerodynamic characteristics of vertical axis turbines is developed in this study. In order to achieve this, a computational domain constructed on moving mesh system is used and flow equations are discretized using finite volume method (FVM). Commonly used turbulence models such as standard k-ε and RNG k-ε turbulence models are used to simulate turbulent flow. The numerical model is validated with wind tunnel experimental data and then it is used to predict flow characteristics and performance of the turbine.

2. Aerodynamic analysis of straight-bladed Darrieus-type vertical axis wind turbine

The vertical axis straight blade wind turbine has a very simple design but its aerodynamic analysis is complex. Many researchers developed several mathematical models for predicting performance and design on Darrieus type vertical axis wind turbines (Islam *et al*. 2008). The most validated and commonly used are assigned in three categories:

i. Momentum model
ii. Vortex model
iii. Cascade model

Furthermore there are some mathematical expressions which are commonly used in most of the aerodynamic models as described below.

The tangential and normal forces on the vertical axis wind turbine blade depend on an angle "α" as seen in Fig. 1.

The average tangential force on one blade can be expressed as

$$F_{ta} = \frac{1}{2\pi}\int_0^{2\pi} F_t(\theta) d_\theta \tag{1}$$

Hence the total torque, T, can be calculated for an "N" number of blades as

$$T = NF_{ta}R \tag{2}$$

Where N is the number of blades, and R is the radius of the turbine. Finally, the total power output is expressed as

$$P = T\omega \tag{3}$$

where ω is the angular velocity.

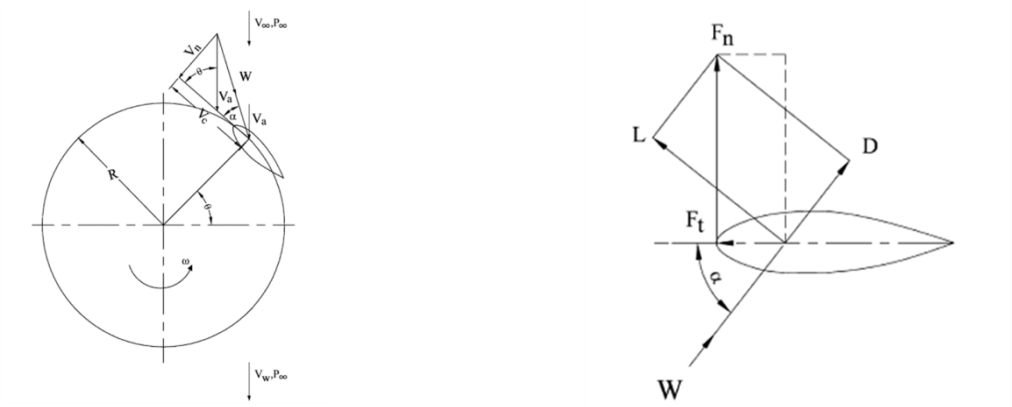

(a) Flow velocities of straight-bladed Darrieus-type VAWT

(b) Force diagram of a blade airfoil

Fig. 1 The tangential and normal forces on the vertical axis wind turbine blade (Islam *et al.* 2008)

3. Computational principles

The present computational study is conducted using a moving mesh technique which is incorporated with a FVM based fluid flow solutions through the commercial software package FLUENT (ANSYS 2009) (ANSYS Inc., Canonsburg, Pennsylvania). The computational domain is comprised of two zones namely; rotating zone in the wake region and stationary fluid zone outside. The unsteady 2-D and 3-D governing flow equations i.e., continuity equation and the Navier-Stokes equations are solved together with the transport equations for the turbulence kinetic energy and its dissipation rate to fully resolve the turbulence flow characteristics.

3.1 Governing equations

The fluid flow is assumed to be incompressible, Newtonian and non-isothermal. The flow equations are conservation equations for mass and momentum. The mass or continuity equation in the general form is described below

$$\frac{\partial \rho}{\partial t} + \nabla(\rho \vec{v}) = 0 \tag{4}$$

Where ρ is density, $\vec{v}$ is velocity vector field, t is time, and the equation is applicable for compressible and incompressible flows. The momentum equation for an inertial reference frame in conservation form and neglecting the curvature and surface tension is described by

$$\frac{\partial}{\partial t}(\rho \vec{v}) + \nabla(\rho \vec{v}\vec{v}) = -\nabla p + \nabla(\bar{\tau}) + \rho \vec{g} + \vec{F} \tag{5}$$

Where, p is the static pressure, $\bar{\tau}$ is the stress tensor (as described below), $\rho\vec{g}$ and $\vec{F}$ are the gravitational body forces and external body forces respectively. The stress tensor is expressed as

$$\bar{\tau} = \mu\left[\left(\nabla\vec{v} + \nabla\vec{v}^{T}\right) - \tfrac{2}{3}\nabla\vec{v}I\right] \tag{6}$$

Where, μ is the molecular viscosity, and I is the unit tensor. In addition to conservation equations for mass and momentum, sliding mesh technique is incorporated with the present FVM based fluid flow solver (ANSYS 2009) to better visualize and capture the unsteady flow characteristics in a rotating frame on the blades surfaces. The equations of motion are modified to include moving motion of the blades and to incorporate the acceleration terms which occur due to the transformation from the stationary to the moving mesh.

The sliding mesh technique is a special case of general dynamic mesh motion where the nodes move rigidly in a given dynamic mesh motion (ANSYS 2009). The grid is divided into two main regions; one attached to a rotating geometry and the other attached to the stationary boundaries of the flow, which slides relative to one another along a slip plane (Bakker *et al*. 2000). In this case all the boundaries in a mesh zone and nodes move together in a rigid fashion without any deformation of the cells.

The general conservation equation formulation for a general scalar, Φ, for dynamic meshes is applied in sliding mesh and described as

$$\frac{d}{dt}\int_{v}\rho\Phi dV + \int_{\partial V}\rho\Phi\left(\vec{u} - \vec{u}_{g}\right)d\vec{A} = \int_{\partial V}\Gamma\nabla\phi d\vec{A} + \int_{V}S\phi dV \tag{7}$$

Where ρ is the fluid density, $\vec{u}$ is the flow velocity vector, $\vec{u}_{g}$ is the mesh velocity of the moving mesh, Γ is the diffusion coefficient, S_{Φ} is the source term of ϕ and ∂V is used to represent the boundary of the control volume, V.

A stationary frame is referred to track the movement in the sliding mesh formulation; consequently the time rate of change of the cell volume is zero

$$V^{n+1} = V^{n} \tag{8}$$

According to the first order backward difference scheme (Jiangtao *et al*. 2012)

$$\frac{d}{dt}\int_{V}\rho\phi dv = \frac{\left[\left(\rho\phi\right)^{n+1} - \left(\rho\phi\right)^{n}\right]v}{\Delta t} \tag{9}$$

Where, n is the present time step, $n+1$ is the next time step.

It is noted here that the solutions with the above equation will be inherently unsteady since the mesh moves.

3.1.1 Reynolds Averaged Navier–Stokes (RANS) based two-equation turbulence models

For turbulent, incompressible and Newtonian viscous fluid, the Reynolds-averaged Navier–Stokes equation is given by

$$\rho \frac{D\bar{u}_i}{Dt} = -\frac{\partial \bar{p}}{\partial x_i} + \frac{\partial}{\partial x_j}\left[\mu\left(\frac{\partial \bar{u}_i}{\partial x_j} + \frac{\partial \bar{u}_j}{\partial x_i} - \frac{2}{3}\delta_{ij}\frac{\partial \bar{u}_i}{\partial x_i}\right)\right] + \frac{\partial}{\partial x_j}\left(-\rho\overline{u_i' u_j'}\right) \tag{10}$$

Where ρ is the fluid density, $\bar{u}_i$ is the time averaged velocity, u_j' is the deviation from the time averaged velocity, p is the time averaged pressure, μ is the dynamic viscosity of the fluid, $-\rho\overline{u_i' u_j'}$ is the Reynold's stress tensor, which appears on the right-hand side of the time-averaged Navier–Stokes equations as a result of time averaging to Navier–stokes equations. The temporal and spatial co-ordinates correspond to t and x_j, respectively. In an eddy-viscosity model, the Reynolds stress is assumed to be proportional to the mean velocity gradients, with the constant of proportionality being the turbulent viscosity, μ_t. This assumption is known as the Boussinesq eddy-viscosity hypothesis, and provides the following expression for the Reynolds stresses (Hinze 1975).

$$-\rho\overline{u_i' u_j'} = \frac{2}{3}\rho k\delta_{ij} + \mu_t\left(\frac{\partial \overline{u_i}}{\partial \overline{x_j}} + \frac{\partial \overline{u_j}}{\partial x_j}\right) + \frac{2}{3}\mu_t\frac{\partial \overline{u_j}}{\partial x_j}\delta_{ij} \tag{11}$$

where k is the turbulent kinetic energy expressed as

$$k = \frac{1}{2}\overline{u_i' u_i'} \tag{12}$$

3.1.2 The standard k-ε turbulence model

The standard k-ε turbulence model is based on transport equations for turbulent kinetic energy k and its dissipation rate, ε, and it is firstly developed by Launder and Spalding (1974). The Standard $k-\varepsilon$ turbulence model is widely used and in the derivation it assumes that the flow is highly turbulent and furthermore the effects of the molecular viscosity are negligible. The turbulence kinetic energy, k and its rate of dissipation, ε are obtained from the following transport equations

$$\rho\frac{Dk}{Dt} = \frac{\partial}{\partial x_i}\left[\left(\mu + \frac{\mu_t}{\sigma_k}\right)\frac{\partial k}{\partial x_i}\right] + G_k - \rho\varepsilon \tag{13}$$

$$\rho\frac{D\varepsilon}{Dt} = \frac{\partial}{\partial x_i}\left[\left(\mu + \frac{\mu_t}{\sigma_\varepsilon}\right)\frac{\partial \varepsilon}{\partial x_i}\right] + C_{1\varepsilon}\frac{\varepsilon}{k}G_k - C_{2\varepsilon}\rho\frac{\varepsilon^2}{k} \tag{14}$$

Where, μ_t is the eddy viscosity, $C_{1\varepsilon}$ and $C_{2\varepsilon}$ are constants in the sense that they are not changed between calculations. σ_k and σ_ε are the turbulent Prandtl numbers for k and ε, respectively. The default values for these coefficients are given as follows: $C_{1\varepsilon} = 1.44, C_{2\varepsilon} = 1.92$, $C_\mu = 0.09, \sigma_k = 1.0$, and $\sigma_\varepsilon = 1.0$. G_k represents the generation of turbulent kinetic energy due to the mean velocity gradients, calculated in a manner consistent with the Boussinesq hypothesis.

3.1.3 The RNG k-ε turbulence model

Further development and Improvement from the standard model has been done by Yakhot *et al.* (1992) and is based on the renormalized (RNG) group theory. An additional sink term is suggested; over the standard *k-ε* turbulence model, in the turbulence dissipation equation to account for non-equilibrium strain rates and employs different values for various model coefficients.

The equation of *k* remains the same and the dissipation equation *ε* is modified to include the additional sink term

$$\frac{C_\mu \eta^3 (1-\eta/\eta_0)}{1+\beta\eta^3}\frac{\varepsilon^3}{k} \tag{15}$$

3.1.4 The k-ω turbulence model

The *k-ω* model is based on Wilcox (1998). It compromises modifications for low Reynolds number effects, compressibility and shear flow spreading. It is characterized by the turbulent kinetic energy and the frequency, $\omega = k/\varepsilon$, where ε is the rate of dissipation of *k*. The turbulence viscosity can be expressed as

$$\mu_t = C_\mu \frac{\rho k}{\omega} \tag{16}$$

The turbulent kinetic energy, *k*, and the specific dissipation rate, ω , are obtained from the following transport equations:

$$\frac{\partial \rho k}{\partial t} + \frac{\partial \left(\rho \overline{u_i} k\right)}{\partial x_j} = \frac{\partial}{\partial x_j}\left[\left(\mu + \frac{\mu_t}{\sigma_k}\right)\frac{\partial k}{\partial x_j}\right] + P - \rho\omega k \tag{17}$$

$$\frac{\partial \rho \omega}{\partial t} + \frac{\partial \left(\rho \overline{u_i} k\right)}{\partial x_j} = \frac{\partial}{\partial x_j}\left[\left(\mu + \frac{\mu_t}{\sigma_w}\right)\frac{\partial \omega}{\partial x_j}\right] + \gamma\frac{\omega}{k} - \beta\rho\frac{\omega^2}{C_\mu} \tag{18}$$

3.2 Geometry set up

Darrieus wind turbines and the modified H-rotor wind turbines are known for using airfoils generating lift to provide rotation. Most of vertical axis wind turbines are using symmetrical four digits NACA airfoils such as NACA0012, 0015, 0018, 0022 and 0024 (Clarck 1991, Beri and Yao 2011). The NACA 4 digits cambered airfoils are tested in previous research (Beri and Yao 2011). It is numerically shown that camber airfoils have the potential to self-start if they are used for vertical wind axis wind turbines. However, the power coefficient of the simulated model showed a reduction in peak efficiency when compared with the conventional non-self-starting airfoils (Beri and Yao 2011). Other advantages of NACA four-digit are, good stall characteristics, small center of pressure movement across large speed range and negligible effect of surface roughness of airfoil (Scott 2001).

In the present study, the geometry is created using a design tool called CATIA V5R20. Symmetrical straight bladed NACA0022 is selected to be the airfoil with 22 mm of thickness, resulting in a 100 mm blade chord. The selection is made in accordance with the vertical axis wind turbine created by Howell *et al*. (2010) for validation purposes with the existing experimental results. The diameter and the overall domain length in the flow direction are set to 0.6 m and 15 m

(25*D*), respectively. This is due to the fact that the effect of the boundary conditions and the wall functions should be kept to minimum to reduce the error factor and also to examine the flow in the wake of the blades. The sides of the domain are considered to be walls to represent the similar physical wall boundary constraints to those in the wind tunnel. The same square tube section of the computational wind tunnel test area of 1.2 m x 1.2 m is employed as in the wind tunnel experiment. The inlet and outlet on the other hand are positioned further away to allow a full development of the wake of the turbine as shown in Fig. 2.

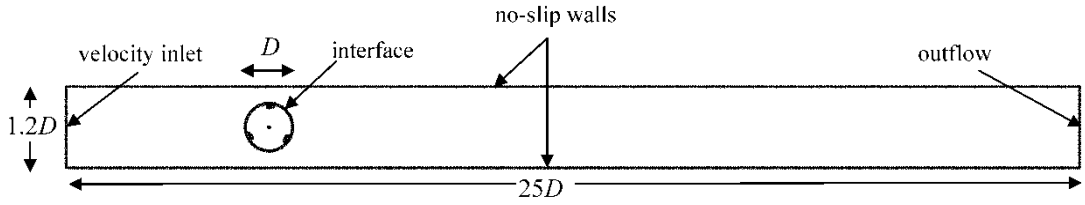

Fig. 2 The model geometry set-up and the computational boundary conditions set-up

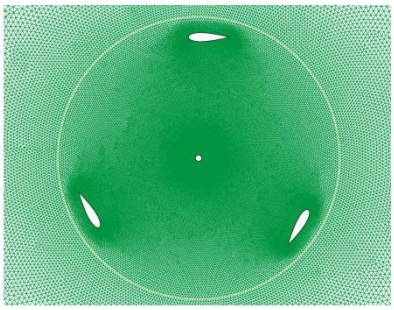

(a) Rotating sub-domain

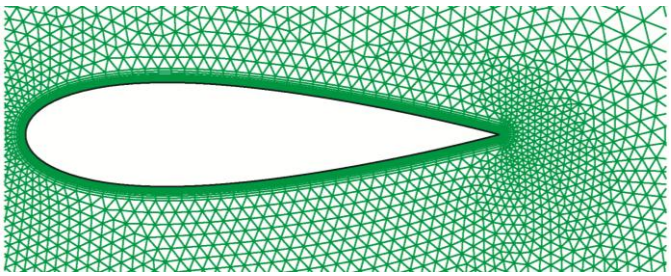

(b) Mesh near Naca0022 Blade

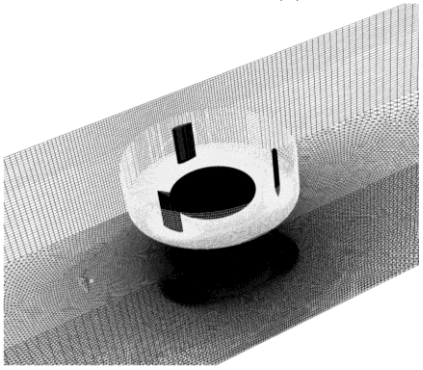

(c) 3-D domain mesh set-up surrounding inner rotating zone.

Fig. 3 The computational mesh set-up

3.3 Computational domain and boundary conditions

The computational domain is constructed using a pre-processor module (Gambit V.5) after building the geometry in CATIA. A cylinder with diameter of 0.7 m is generated in Gambit to set up a rotating zone and finer mesh could be created in the center of the circle and less mesh cells would be used in the outer volume as illustrated in 2-D mesh layouts of the present flow domain together with the 3-D local mesh representing the rotating inner zone and stationary outer zone as shown in Fig. 3. The mesh should be fine close to the blades to accurately simulate the large velocity and pressure gradients within the boundary layer. It is ensured that the mesh with y^+ values of less than 4 would be achieved for accurate simulation of flow within the turbulent boundary layer for enhanced wall treatment and y^+ values between 20 and 130 for the standard wall treatment (ANSYS 2009). Whereas within the stationary outer region, the flow would settle down after the wake of the turbine and relatively less number of cells would be enough to simulate the flow characteristics. Therefore overall mesh size is optimized to use less computational time and memory for the present simulations.

The interface zone is initially set to correspond to one degree counter of clockwise rotation (in the case of transient calculations) and then to vary the rotational angle to examine the most efficient case, where minimum nodes with high efficiency would be achieved. With a full 360 degrees rotation and an angle of rotation of one degree the required nodes to be set to the interface will be 360°. But according to previous numerical study of Beri and Yao (2011), two degrees or more can be set with minimum effect of the overall computation. Ideally it would be preferable to set the minimum set of degrees and hence more accuracy but this is conflicting with the fact that more computational memory and time are needed and this is expensive and limited in most cases.

The low mesh resolution comprised of 45 nodes is initially adopted on the airfoils edge to observe where more cells would be required for a realistic representation of the airfoil shape. It is noticed that the airfoil shape is lost without using a high number of grid nodes especially on the curvature section of the airfoil. Therefore, more number of nodes is used on the curvature section of the airfoil to maintain the airfoil shape with a total number of 100 nodes on the airfoil edge. On the other hand, a size function is applied to capture the correct curvature without exceeding the number of nodes on the blades. An angle of 6 degrees is selected with a 1.2 growth factor resulting in a 100 nodes on each blade.

The domain is created using triangular blocks, and for the steady outer sub-domain a size function in Gambit is applied to focus more cells when approaching the center and where it is needed more (Fig. 3). The blades are attached by imaginary rotor arms at the aerodynamic center of ¼ from the leading edge of the airfoil blade.

Following the set-ups for the model geometry and the computational domain, the boundary conditions are imposed at the boundaries of the computational domain as illustrated in Fig. 2. Velocity inlet is introduced as inlet of the domain while outflow boundary condition is applied to the outlet of the flow domain as it is shown in Fig. 2. The inflow velocity with a normal vector to boundary magnitude direction is specified at the inlet with turbulence boundary conditions (the turbulence intensity of 1% and length scale of 0.01 m) specified in accordance with the experimental study while outflow boundary condition with outflow flow rate of 1 is imposed to represent a fully developed velocity boundary condition there. A sliding mesh boundary condition is also provided to represent the rotation of the inner domain over a stationary outer domain with a generation of mesh interface between these two zones. The mesh interface is created by the two interfaces of the steady and rotating sub-domains to provide the sliding mesh, and the angular

velocity is set on the moving mesh at the required rotating zone. Because the mesh motion in the sliding mesh formulation is rigid, all cells in the rotating zone retain their original shape and volume except its rotational movement in the counter clock wise direction with a specified angular velocity. The blades are set as rotating no-slip walls but without any roughness effect as in this case the roughness is considered to be negligible. At the sidewalls of the wind tunnels, no-slip boundary condition is also imposed and in the vicinity of these boundaries in the streamwise direction a boundary layer mesh accompanied with the enhanced wall treatment case (i.e., no wall function approach) is employed. This is desirable to control the evolution of the y^+ values along the wall surfaces. The first cell height is set to 0.25 mm with a growth factor of 1.6 for a total number of 9 layers. Initial mesh independency tests are performed by using two different simulation cases of the same boundary conditions for different mesh resolutions with their accompanied different wall treatments.

3.4 Solution method

The pressure based numerical algorithm with the pressure-implicit with splitting of operators (PISO) - pressure velocity coupling scheme (Issa 1986) - based on the high degree of approximate relation between pressure and velocity is used with second order up-winding numerical error scheme after 5th revolution to maintain more accuracy. The solution convergence criterion is set to 0.0001 for all solution variables.

Due to previous studies (Beri and Yao 2011, Howell *et al*. 2010, Yao 2012) on various turbulence models, it is concluded that the RNG k-ε turbulence model with standard wall functions would be the best suitable turbulence model for this case. The main criterion of the turbulence model selection is further comparatively analyzed with use of different RANS based two equation turbulence models in the subsequent section (Section 4). All the time-averaged computations for the coefficients namely power-coefficient and moment coefficient are performed once the simulation reached statistically steady state condition. It is observed that after about five revolutions the flow field becomes periodically stable as illustrated in Fig. 4. The time averaged total power coefficient over five revolutions represents a statistically steady value.

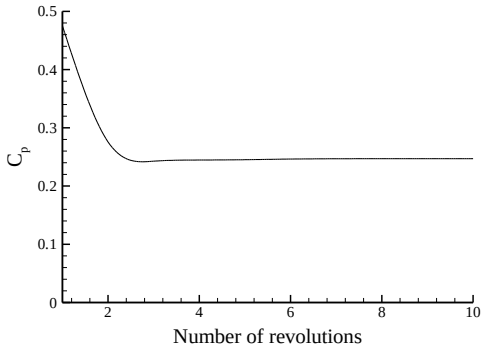

Fig. 4 The power coefficient against revolutions for inflow wind velocity of 5.07 m/s and TSR of 2.27 TSR at 0-degree design AOA

Table 1 Comparative summary of calculated average moment coefficient values in comparison with the experimental data for inflow wind velocity of 5.07 m/s at TSR of 2.15

	Flow dimension	Mesh resolution (#nodes)	Power Coefficient (C_p)
Standard k-ε	2-D	68,000	0.144631
RNG k-ε	2-D	47,900	0.052417
RNG k-ε	2-D	56,100	0.327659
RNG k-ε	2-D	68,000	0.307902
Standard k-ω	2-D	68,000	0.050456
RNG k-ε	3-D	3,616,000	0.229496
Experiment			0.21

4. Simulation cases and validation

A number of simulations are performed and compared with experimental data to validate the numerical solution technique. Initially, a mesh independency test is conducted with three different mesh resolutions ranging from 47,900 to 68,000 nodes for RNG k-ε turbulence model.

As shown in Table 1, the total average value of the power coefficient is highly dependent upon the mesh resolution as well as the choice of the turbulence model. The power coefficient predicted using RNG k-ε turbulence model with the finest mesh resolution of 68,000 nodes for wind velocity of 5.07 m/s and TSR of 2.15 is in good agreement with the experimental data. As expected the coarse mesh (47,000 nodes) could not capture the turbulent flow characteristics accurately due to lack of cell resolution. The predicted value for the 3-D mesh configuration of total nodes of 2.4 million grid nodes is even more correlated with the experimental value. However, the total CPU time for the 3-D simulation is 84 hours for one complete revolution of the turbine rotor on 12 processors (Sun Fire X2200 M22xOpteron 2218, 12x2GB ECC DDR-667 RAM) cluster computer using parallel computing technology. Therefore the parametric study is performed using 2-D simulations in order to reduce the total computational time.

Since the choice of the first grid cell height is also influential in terms of determining the required y^+ value for no-wall function and/or standard wall function application, the distribution of the first grid cells from the wall surfaces is examined to ensure that the evolution of y^+ value could meet the requirement for both applications. This examination with different mesh configurations and mesh size functions concluded that the first grid cell arrangement in the vicinity of the all wall surfaces could be better satisfied for the standard wall function approach compared with no-wall approach of enhanced wall treatment for the specified y^+ distribution range for both approaches. Therefore, the parametric study is completed with the standard wall function approach in conjunction with the chosen turbulence model in the further stage.

In addition to the mesh independency test, the modeling effects on the evolution of power coefficient are also investigated for the standard k-ε turbulence model, k-ω turbulence model and RNG k-ε turbulence model with mesh size of 68,000 nodes (Table 1).

It is observed that the better coefficient result for the power coefficient could be predicted with the RNG k-ε turbulence model than other standard turbulence models. The flow physics obtained from each turbulence model case is also analysed in qualitative manner and the simulation differences are presented in terms of instantaneous vorticity contours in the wake of the rotating sub-domain in Figs. 5(a) to 5(c).

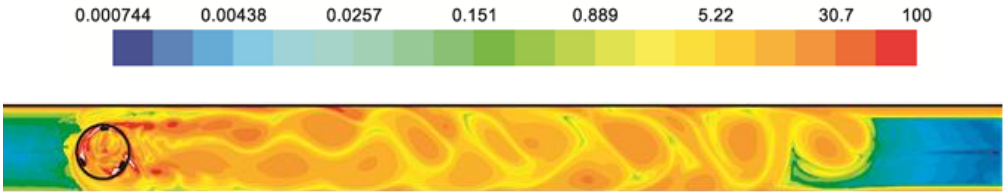

(a) RNG k-ε turbulence model

(b) Standard k-ε turbulence model

(c) Standard k-ω turbulence model

Fig. 5 Instantaneous vorticity contours on the wake for different turbulence models for inflow wind velocity of 5.07 m/s and TSR of 2.15 at 0-degree design AOA

Figs. 5(a) to 5(c) clearly illustrate the differences in occurrence of the vortex street behind the rotating sub-domain for each turbulence model case. The less elongated separated shear layer in case of the RNG k-ε model leads to stronger and more discernible vortex patterns in the wake compared to those for the other two standard turbulence model cases, which reproduce more elongated separated shear layers rolling into very weak and less discernible vortex patters as seen in Figs. 5(b)-5(c). The more stronger and distinguished coherent structures (swirling patterns) could be probably attributed to the main cause of higher velocity and pressure field changes in the rotating domain which lead to higher lift and torque compared with other two model cases. The periodic motion in the wake therefore is highly underestimated by these later standard models.

Figs. 5(a)-5(c) also signify the strong blockage effects on the evolution of the separated shear layer region and the formation of the vortices in the wake region for each turbulence model. The blockage causes the flow characteristics to vary from those expected in full scale undisturbed flow situations without wall constraints. Therefore, an accurate quantitative knowledge of the computational and/or experimental wind tunnel blockage effect would be essential before any comparison and prediction work on wind turbine response could be pursued. However, due to the fact that the estimation of the correct value of wake blockage is rather difficult computationally the blockage effect is not considered in the present computations in accordance with the experimental study (Howell *et al*. 2010). Therefore, no correction is introduced into the calculation of the force and moment coefficients for making direct comparison with the experimental values. However, for more accurate predictions of power and moment coefficients these effects should be taken into

consideration.

The test conditions for parametric study are summarized in Table 2. The difference between one degree of rotation and two degrees of rotation is minor therefore the two degree of rotation could be used to reduce overall computational time. A pressure based segregated PISO numerical algorithm together with PRESTO pressure-velocity coupling scheme results in a more stable convergence even with a large time step size when compared with SIMPLE and SIMPLEC schemes. The predicted values for power coefficients are also in a better agreement with experimental data for the PISO scheme.

Table 2 Simulation Test Cases – Model set-up comparison at inflow wind velocity of 5.07 m/s and TSR of 2.15 for 0-degree design AOA

Wall Treatment	Scheme	Pressure	Deg	C_p
Enhanced	Simple	Std	2	0.33822
Enhanced	Simple	Std	1	0.34183
Standard	Simple	Std	2	0.11979
Enhanced	Simple	Presto	2	0.33456
Enhanced	SimpleC	Presto	2	0.32776
Enhanced	Piso	Presto	2	0.32766
Standard	Piso	Presto	2	0.39280

This solver set-up is adopted for the further parametric study. Having decided the choice of turbulence model and its solver-set up for the finalized computational mesh and geometry constraints, a parametric study is performed for different tip-speed ratios (TSR), wind inflow velocities and mounted angle of attacks in accordance with the experimental parameters of Howell *et al*. (2010). Table 3 summarizes the flow conditions for inflow wind velocity of 5.07 m/s for different TSRs at 0-degree design AOA.

Table 3 Flow conditions for inflow wind velocity of 5.07 m/s for different TSRs at 0-degree design AOA

TSR (λ)	Velocity (m/s)	Angular velocity (rad/s)	Time step size(s)	Re	Intensity
1.85	5.07	31.265	0.00111647	64,243	0.040
2.15	5.07	36.335	0.00096069	74,661	0.039
2.27	5.07	38.363	0.00090990	78,828	0.039
2.4	5.07	40.56	0.00086062	83,342	0.039
2.45	5.07	41.405	0.00084305	85,079	0.039
2.57	5.07	43.433	0.00080369	89,246	0.038

The time step size as mentioned earlier is set corresponding to two degree rotation for each rotational speed of the rotor (ω), and the maximum iterations are set for sixty. The tip-speed ratio is set between 1 and 2.55, but for the purpose of angle of attack comparison, the tip speed ratio is set at 2.15 corresponding to all mounted angle of attack. The value of tip-speed ratio (TSR) is varied by assigning different constant values to the angular velocity (ω) and the free stream

velocity (V_∞) for the same radius of the turbine for each simulation condition as below

$$TSR = R\omega / V_\infty \tag{19}$$

5. Results and discussion

Two and three-dimensional transient, turbulent incompressible simulations with a moving mesh technique over 10 revolutions of the inner sub-domain to represent the rotor motion are performed. The power performance of the turbine model is analyzed for a range of wind inflow velocities, TSR and mounted angle of attacks (AOA)

The results are represented quantitatively in terms of moment coefficient and qualitatively in terms of velocity vectors and pressure field to illustrate basic flow feature and changes in the flow features that occur during the revolution of the rotor model.

The blade aerodynamic forces are computed by integrating pressure and shear stress over each blade surface. The total torque of the turbine is obtained by simply adding the three blade force components and torque and is averaged for each revolution of the turbine to determine the dynamic torque of the turbine (Beri and Yao 2011). These values are finally used to calculate the power coefficient, C_p with the following equation

$$C_p = \frac{P}{0.5\rho A V^3} \tag{20}$$

For applying the reference values for the projected area, uniform wind inflow velocity and the radius of the turbine, the moment coefficient, C_m is also computed with the below equation

$$C_m = \frac{T}{0.5\rho V^2 AR} \tag{21}$$

Table 4 below summarizes the computed average power coefficients in comparison with the experimental values obtained at inflow wind velocity of 5.07 m/s for different TSRs at 0-degree design AOA. The discrepancy between the computed and experimental values increases as the TSR value increases.

Table 4 The calculated power coefficient, C_p comparison at inflow wind velocity of 5.07 m/s for different TSRs at 0-degree design AOA

TSR	Angular vel. (rad/s)	Experimental C_p	Computational C_p
1.85	31.265	0.19	0.223386
2.15	36.335	0.21	0.244156
2.27	38.363	0.2	0.247072
2.45	41.405	0.17	0.225978
2.5	42.25	0.15	0.217855

The graphical representations of the computed averaged C_p values with respect to the TSRs for

different inflow velocities are provided in Figs. 6(a) and 6(b). It is seen in these figures that the correspondence between the computed results and the experimental data is acceptable at low TSR values considering the fact that simulations are performed in 2-D manner with a few geometric simplifications.

However, the relative error between the computed and experimental values increases at higher TSR values due to more intensifying non-linear interactions between the inner rotating domain and its periodic near wake region which could not be captured well with the present RANS based simulations because RANS schemes inherently predict average flow conditions. The mass of the rotor arms, which may have some influence on the prediction of lift produced by the blades and the shaft condition (stable or rotating) are not taken into consideration in these 2-D simplified simulations. The effects of tip-vortices are also three-dimensional. It is stated that the 2-D simulations using RNG k-ε turbulence model is not capable of fully capturing the 3-D effects at higher TSRs.

The effect of mounted angle of attack (AOA) is also studied for different AOA values for a simulation case with inflow wind velocity of 5.07 m/s at TSR of 2.15. The results are presented in terms of the distribution of the computed average power coefficient and moment coefficient in Figs. 7(a) and 7(b), respectively. It should be noted here that the mounted angle of attack is changed for every blade with a fixed rotation angle(s) of the blade and the total average torque is determined under specified constant TSR value of 2.15 for each simulation case. These torque measurements are also repeated every 5-degrees of the blade rotation i.e., AOA up to maximum AOA of 20 degrees for a specified TSR of 2.15 to investigate the effect of AOA on the power and moment coefficient results. The total torque as described above is obtained by adding the forces of the blades and then averaging for each revolution before settling. It is observed from Figs. 7(a) and 7(b) that at a mounted angle of attack ranges from 5 to 10 degrees, the torque and power outputs reach their unique maximum local values before decreasing again. The change in AOA significantly affects the pressure distribution (as later shown in Figs. 10 and 12) in rotating sub-domain leading to variations in the performance of the turbine.

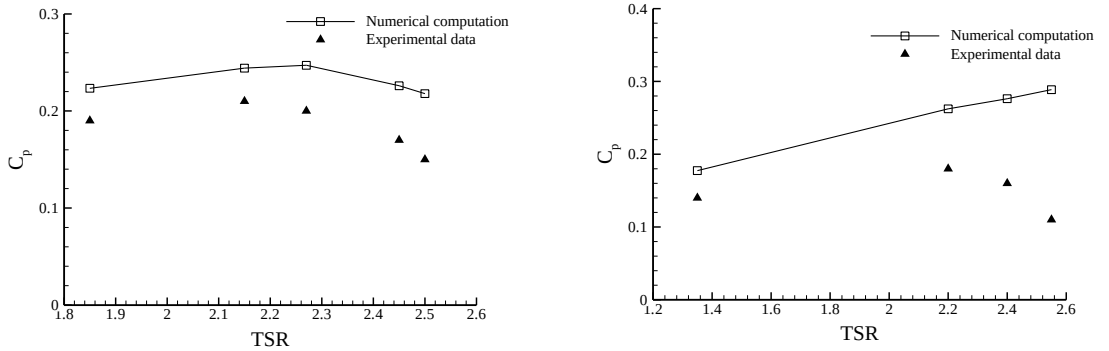

(a) Inflow wind velocity of 5.07 m/s inlet velocity at 0-degree design AOA

(b) Inflow wind velocity of 4.31m/s at 0-degree design AOA

Fig. 6 Power coefficient comparison with the experimental data at different TSR values

(a) Power coefficient at different AOAs (b) Moment coefficient at different AOAs

Fig. 7 Power and torque performance of turbine against mounted angle of attack for inflow wind velocity of 5.07 and TSR of 2.15

The turbine is rotated in the counter-clockwise direction and the all blades do not always produce lift simultaneously. This is probably due to the fact that the blades can interfere with each other. The blades facing the wind flow at windward faces have a negative impact on the blades on the leeward side (azimuthal angle 180-360) resulting in a negative torque output as later can be seen in Fig. 9(c).

The dynamic moment coefficient for each blade and sum of the blades is determined instantly and its evolution for the last 5 revolutions (periods) of the rotor sub-domain are represented in Figs. 8(a) and 8(b). Fig. 8(a) clearly demonstrates a periodic nature of the moment coefficient with small negative values arising some concerns about the self-starting capabilities of the present VAWT model. The evolution of the same coefficient for each blade and the sum of the blade is further represented in Fig. 8(b) to make a direct comparison for each blade performance. It is also seen in this figure that at the constant speed of the inflow wind and the rotation, the total torque of the present turbine model (summation of each blade's moment value) would also represent a perfect periodic nature for the last 5 revolutions with an indication of a stable condition with a resultant positive average value as seen for each blade.

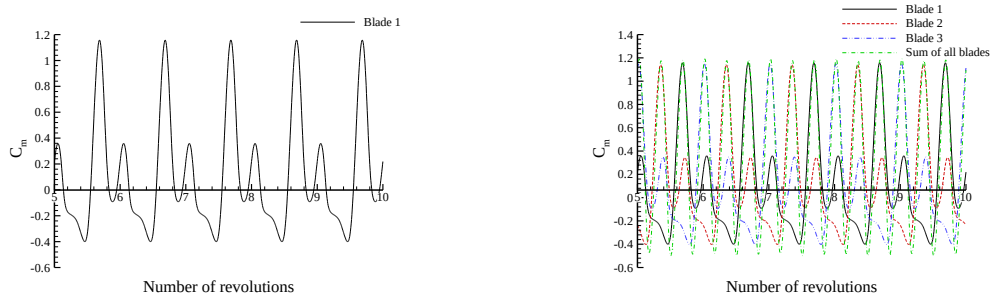

(a) Single blade (b) All blades

Fig. 8 Sum of all blades performance in terms of moment coefficient for the last 5 revolutions of for inflow wind velocity of 5.07m/s and TSR of 2.15 at 0-degree design AOA

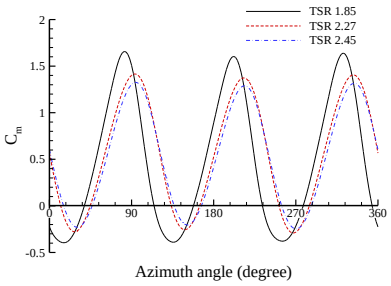

(a) Different TSR performance comparison at 0-degree design AOA

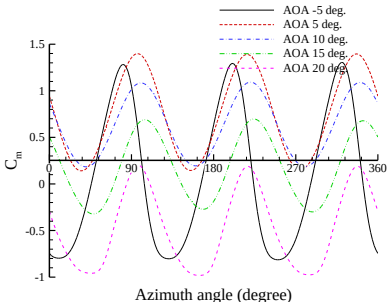

(b) Different AOAs at TSR of 2.15

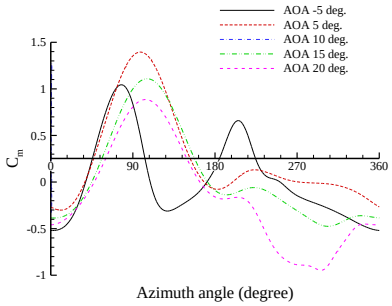

(c) Single blade at different azimuthal positions at different AOAs at TSR of 2.1

Fig. 9 The evolution of the moment coefficient at different azimuth positions at inflow velocity of 5.07 m/s

Fig. 8(b) also indicates that the total moment coefficient, which is the sum of all the blades at each time step also has negative value which shows that the self starting cababilities are not good for this turbine.

The evolution of total moment coefficient is also determined for a complete one rotational period with different azimuthal angles for different TSR values to better analyse the negative instantaneous values and their influence on the output power (Figs. 9(a) to 9(c)). The average moment coefficient value decreases as the TSR value increases and a slight phase shift is observed for each case. This would be more beneficial for self-starting capabilities of the turbine, however the overall average power coefficient would be reduced. With this respect, the optimum performance between the moment coefficients and power coefficient should be investigated prior to a VAWT manufacture. The lower performance is noticed at azimuthal angles of 30, 150, 270 and 360 degrees.

A positive overall torque can be achieved by having a fixed angle of attack on the blades as shown in Fig. 9(b). This offers a solution to overcome one of the drawbacks of symmetrical blades VAWT and improves its self-starting capability. As seen in Fig. 9 the mounted angles of 5 and 10 degrees reproduce only positive moment coefficient but the performance reduces for the angles of 15 and 20 degrees.

The mounted AOA of 10 degrees reproduce moment coefficient within a smaller range compared to other angles; thereby resulting in less tension on the support arms. This would be more beneficial for structural stability of the turbine. It is noted that AOA of minus 5 degrees

reproduces higher range of all comparative values (Fig. 9(c)). Further analysis of moment coefficient for a single blade with different mounted angles of attack at a complete crown of rotation (2 degrees azimuthal position change at each time step) suggests that the highest moment coefficient is found at the 5 degrees AOA, between 90 and 100 degrees azimuthal angle. All the AOAs have their peak points between 80 and 100 degrees azimuthal angle. In the angles of 5,10,15, and 20 degrees AOA after their peak point, the moment coefficient starts to decrease and another smaller peak before decreasing again. In the case of -5 degrees AOA, the first peak point to the second peak point has the least difference of 0.3 in comparison with the other AOAs.

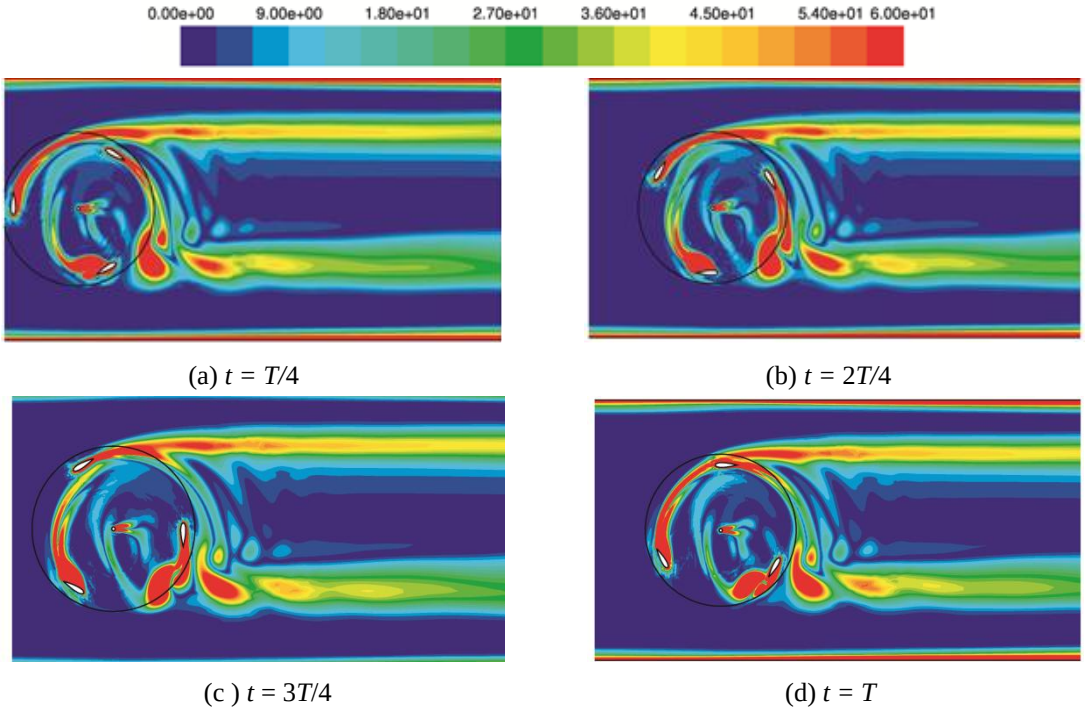

(a) $t = T/4$ (b) $t = 2T/4$

(c) $t = 3T/4$ (d) $t = T$

Fig. 10 Vorticity contours a 4 different time positions concentrated on the rotating domain for inflow wind velocity of 5.07 m/s and TSR of 2.27 at 0-degree design AOA

A better understanding of the behaviour of the blades can be achieved by investigating the performance of a single blade. In Fig. 9(c) it can be seen that for all positive mounted angles of attacks, after 180 degrees of azimuthal angle, the moment coefficients are negative. This is inconsistent with the values of the negative mounted angle of attack. At an angle of -5 degrees better performance (or positive moment coefficients) is achieved between the azimuthal angles of 180 and 270 degrees. Between 90-180 degrees performance is reduced, and at zero and 360 degrees all mounted AOA reproduce negative results. At the specific blade location of an azimuthal position of 0 or 360 degrees, the blade will have a resultant force in the negative direction of the turbine system rotation. This is due to the fact that more lift will be created by the blade, as it directly faces the inflow wind velocity. A suggestion would be, to improve this counter

clockwise rotation turbine system, to place the blade that directly faces the inflow wind at an azimuthal position of 180 degrees. This requires further research and testing to be carried out to estimate the most beneficial blade position. By having each blade independently rotate on their aerodynamic centre (usually ¼ of blade chord) would raise an advantage of system control and generation of positive and smaller range dynamic moment and power coefficients at each blade instantaneous position. Further models should be considered for dynamic blades creation and changeable mounted angle of attack on each blade independently. The desirable models should achieve increase of performance with the same geometry (Hwang *et al*. 2006).

The vorticity contours are presented in terms of the distribution of local vorticity magnitudes in the rotational sub-domain at different equally distributed time intervals of T/4 during the last revolution of the turbine in Fig. 10. Similar vortex patterns in the rotating sub-domain are observed around each blade surface with higher vorticity magnitudes compared with those of near wake. These coherent structures could be considered to be a source of higher velocity and pressure gradients in the rotation sub-domain as observed in the subsequent figures (Figs. 10-13). Two distinct elongated free shear layers which prevail at the upper and lower interface boundaries of the rotating sub-domain and the stationary near wake zone could be also attributed to vortex distortions for the near wake vortex shedding. The separated local fluid zones generated from each blade and rotor shaft are found to be interfering with each other, which in turn affect the performance of each blade.

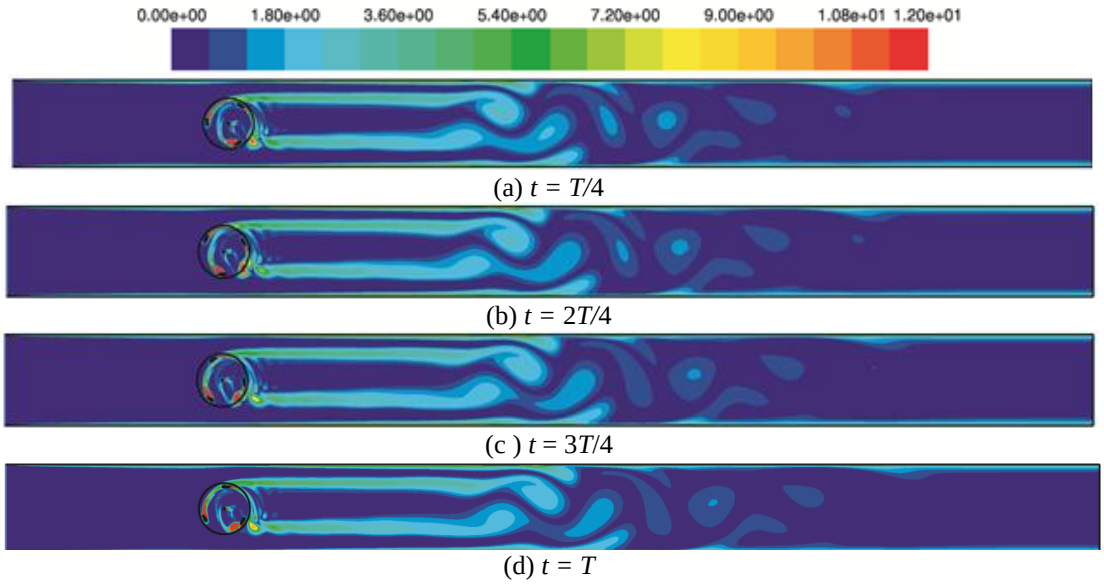

(a) $t = T/4$

(b) $t = 2T/4$

(c) $t = 3T/4$

(d) $t = T$

Fig. 11 Velocity contours at turbine wake at different time periods for inflow wind velocity of 5.07 m/s and TSR of2.27 at 0-degree design AOA

Figs. 11(a)-11(d) on the other hand provide information regarding the wake flow patterns i.e. coherent vortical structures of the rotating sub-domain in the stationary zone at different equally distributed time intervals of $T/4$ again during the last revolution of the turbine. As seen in these

figures, there is a strong influence of wall constraint in the evolution of the separated shear layers from the rotating sub-domain. Their rolling up into vortex patterns in the near wake region is significantly affected and there is a strong convection mechanism between the wake and the separated free shear layer flow further downstream of the flow.

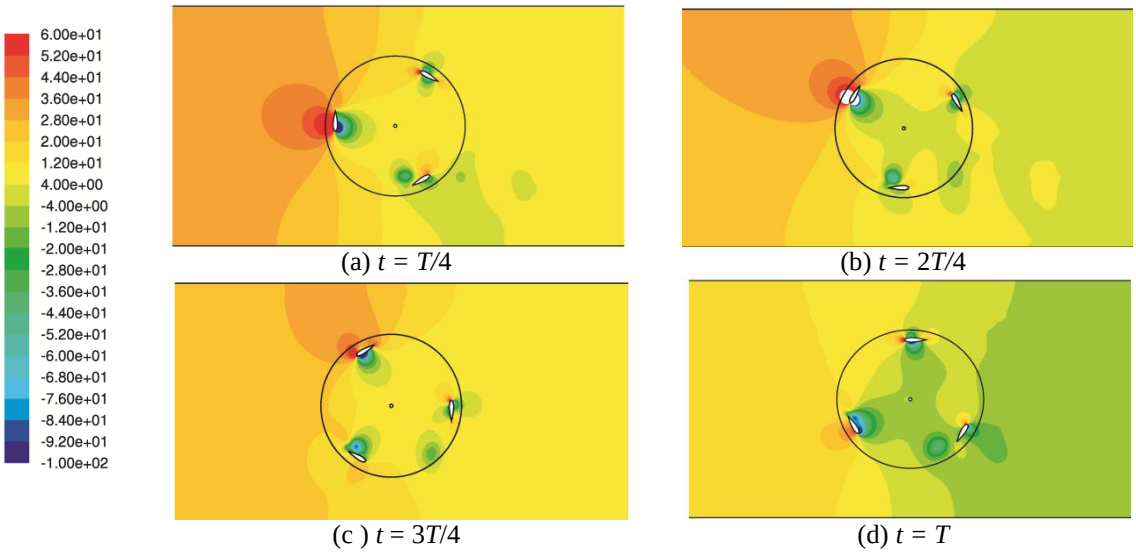

(a) $t = T/4$ (b) $t = 2T/4$

(c) $t = 3T/4$ (d) $t = T$

Fig. 12 Pressure contours at different time periods for inflow wind velocity of 5.07 m/s and TSR of 2.27 at 0-degree design AOA

The time dependent local pressure distribution in the rotating sub-domain is also studied at equally distributed time intervals of $T/4$ shown in Figs. 12(a) to (d). As seen in these figures, the rotor blades have a large effect on the local pressure field in the rotating sun-domain, and the highest pressure distributions is observed at the windward faces of the blades. The lower pressure distribution along the windward face and higher pressure distribution along the leeward face of the blade are clearly identified for each blade. The highest pressure difference is being noted at time instant, $t=T/2$ where the blade moves at 90-100 azimuthal degrees. The higher torque coefficient on all blades is observed at the upwind of the turbine system (azimuthal angles 0-180 degrees) and this is observed where the blades are at a high relative angle of attack (Castelli *et al.* 2011). Furthermore, the variation between local pressure fields around the blades at different time instants gives an indication to these areas in which secondary weak flows would occur due to pressure higher than at the near wake region.

The effect of mounted angle of attack on the velocity and pressure fields with special emphasis on the rotating sub-domain is also investigated briefly and their corresponding instantaneous velocity and pressure fields for inflow wind velocity of 5.07 m/s and TSR of 2.27 and azimuth angle of 90,180,270 and 360 degrees are presented in Figs. 13 and 14, respectively. As seen in these two figures, at a mounted AOA of 15 and 20 degrees, where minimum output performance has been noted, a significant transformation compared with the maximum output performance of 5 and 10 degrees mounted angle at blades 2 and 3 (120 and 270 degrees azimuthal angle) has been

distinguished. Additionally in this case a higher pressure difference and smoother separation are observed (Fig. 15) at the windward facing blades. Moreover different vortex patterns are observed at different mounted AOA on blade 3. Recirculation is distinguished at -5 degree mounted AOA and the pressure difference is greater compared with the positive AOAs, justifying the higher results range of moment coefficients in Fig. 9.

The instantaneous streamlines and velocity vector field in the rotating sub-domain obtained from the 3-D simulation case are finally represented in Figs. 15(a) and (b), respectively as an indication of growing three-dimensionality in the wake of the rotating sub-domain due to pronounced effects of this domain on the near wake in the stationary zone. A clear deviation from two-dimensionality to three-dimensionality around the tip surfaces of the blades could be attained to occurrence of tip vortices leading to significant 3-D effects in this zone and hence the near wake. The large velocity gradient and associated pressure gradient also exit around each blade as observed for 2-D simulation case previously.

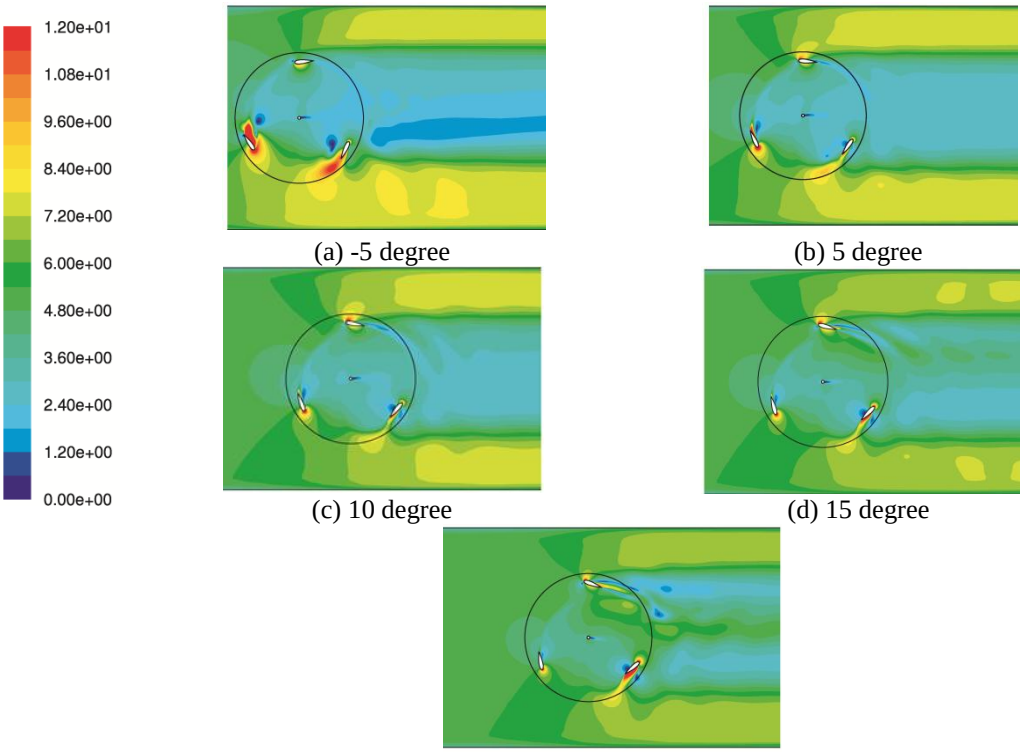

(a) -5 degree (b) 5 degree

(c) 10 degree (d) 15 degree

(d) 20 degree

Fig. 13 Velocity contours for different mounted angle of attack for inflow wind velocity of 5.07 m/s and TSR of 2.27 at azimuthal angle of 0 degree

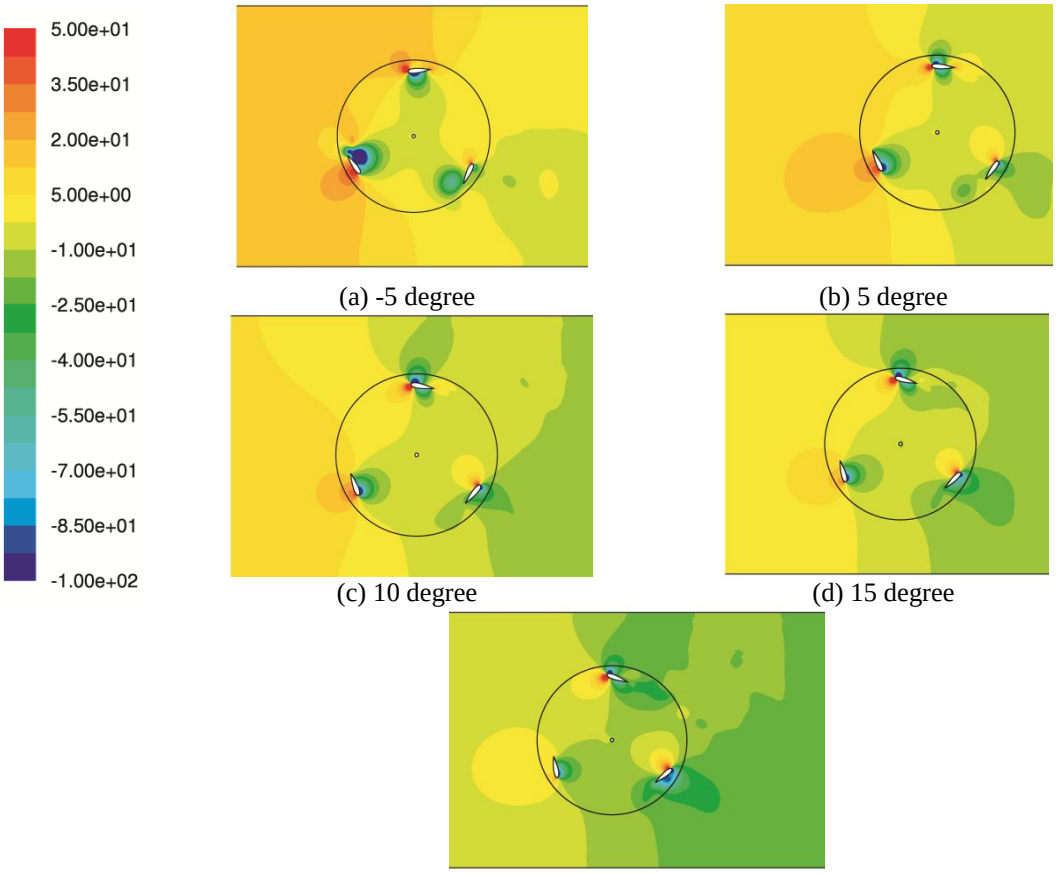

(a) -5 degree (b) 5 degree

(c) 10 degree (d) 15 degree

(d) 20 degree

Fig. 14 Pressure contours for different mounted angle of attack for inflow wind velocity of 5.07 m/s and TSR of 2.27 at azimuthal angle of 0 degree

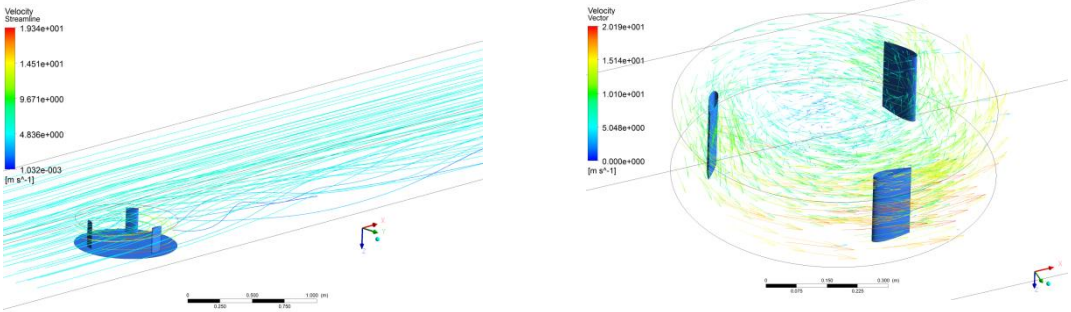

(a) Streamlines (b) Velocity vectors

Fig. 15 Instantaneous 3-D streamlines and velocity vectors passing through the rotational domain at the end of 5th revolution of the rotating domain

6. Conclusions

Overall conclusion form the present work is that the a 2-D model with moving mesh techniques to model blade rotation and RNG k-ε model for turbulence can be used as design tool for evaluating performance of wind turbines. In addition to this further conclusions are as follows:

- The performance of NACA0022 based 3-bladed VAWT turbine system is numerically analysed. It is found that average torque values are positive. However the negative values in the evolution of moment coefficient indicate possible problems related to self-starting-up of the turbine.
- The choice of URANS turbulence model and accompanied near wall treatment influences the numerical resolution of flow field and hence the predictions for the values of moment coefficient C_m, normal force coefficient C_n and power coefficient C_p are affected accordingly.
- It is evident that the wake and the vortex street are highly distorted due to the wall constraints. Further analysis is highly required to take into account of wall blockage effects prior to full scale measurements in the undisturbed environment.
- The analysis of a single blade reveals the performance of the turbine system at different azimuthal positions. It shows that the negative mounted AOA response better for turbine system at the downwind azimuthal positions. Therefore, a combination of AOA and azimuthal position is required to achieve the optimal performance.
- 2-D simulations reproduce acceptable results and predict correct trend of C_m and C_p for different TSRs. However, the predicted values are higher than the experimental data and the discrepancy between the computational and the experimental of about 14%. Therefore, the presented numerical approach is good for parametric evaluations at initial design stages but for final design considerations 3-D simulations are recommended.

References

Ansys (2009), *Fluent theory guide*, V.l3., Ansys Inc.

Bakker, A., LaRoche, R.D., Wang, M.H. and Calabrese, R.V. (2000), *Sliding mesh simulation of laminar flow in stirred reactors*, The Online CFM Book.

Beri, H. and Yao, Y. (2011), "Effect of camber airfoil on self starting of vertical axis wind turbine", *Environ. Sci. Technol.*, **4**(3), 302-312.

Betz, A. (1920), "Das maximum der theoretisch möglichen Ausnützung des windes durch windmotoren", *Zeitschrift für das gesamte Turbinenwesen*, 307-309.

Castelli, M.R., Allesandro, E. and Ernesto, B. (2011), "The darrieus wind turbine: proposal for a new performance prediction model based on CFD", *Energy*, **36**, 4919-4934.

Drees, H. (1978), "The cycloturbine and its potential for broad applications", *Proceedings of the 2nd International Symposium on Wind Energy Systems*, Amsterdam.

El-Samanoudy, M., Ghorab, A. and Youssef, S. (2010), "Effect of some design parameters on the performance of a Giromill vertical axis wind turbine", *Ain Shams Eng. J.*, **1**, 85-95.

Grylls, W., Dale, B. and Sarre, P. (1978), "A Theoretical and experimental investigation into the variable pitch vertical axis wind turbine", *Proceedings of the 2nd International Symposium on Wind Energy Systems*, Amsterdam.

Hau, E. (2006), *Wind turbines- fundamentals, technologies, applocations, economics*, 2nd Ed., Berlin Hetdelberg, Springer.

Hinze, O. (1975), *Turbulence*, New York, McGraw-Hill Publishing Co.

Howell, R., Qin, N., Edwards, J. and Durrani, N. (2010), "Wind tunnel and numerical study of a small

vertical axis wind turbine", *Renew. Energ.*, **35**, 412-422.
Hwang, I., Jeong, I., Lee, Y. and Kim, S. (2006), "Aerodynamic analysis and rotor control of a new vertical axis wind turbine by individual blade control method", *Proceedings of the 17th International Conference on Adaptive*, Taiwan, Oct. 16-19.
Hwang, I.S., Ming, S.Y., Jeong, I.J., Lee, Y.H. and Kim S.J. (2006), "Efficiency improvement of cycloidal wind turbine by active control of the blade motion", *Proceedings of the 16th International Conference on Adaptive Structures and Technologies*, Paris, France, Oct. 9-15.
Issa, R. (1986), "Solution of the implicitly discretized fluid-flow equations by operator-splitting", *J. Comput Phys*, **62**, 40-65.
Jiangtao, L., Jingjing, L., Gang, C. and Yueming, L. (2012), "Numerical simulation method for unsteady aerodynamics of high speed trains", *Int. J. Aerospace Lightweight Struct.*, **1**(2).
Kirke, B. and Lazauskas, L. (1991), "Enhacing the performance of vertical axis wind turbine using a simple variable pitch system", *Wind Eng*., **15**, 187-195.
Mazharul, I., David, S., Ting, K. and Fartaj, A. (2008), "Aerodynamic models for Darrieus-type straight bladed vertical axis wind turbines", *Renewable and Sustainable Energy Reviews,* **12**, 1087-1109.
Clarck, R.N. (1991), "Design and initial performance of a 500 KW vertical axis wind turbine", *Transaction ASAE,* **34**(3), 985-991.
Savonious, S. (1931), "The S-rotor and its application", *Mech. Eng.*, **53**(5), 333-338.
Scott, J. (2001), *NACA Airfoil Series.* [Online]
Available at: http://www.aerospaceweb.org/question/airfoils/q0041.shtml [Accessed 16 October 2010].
Spera, D.A. (1994), *Wind turbine technology*, New York: ASME Press.
Tutar, M. and Holdo A.E. (2001), "Computational modelling of flow around a circular cylinder in sub-critical flow regime with various turbulence models", *Int. J. Numer. Meth. Fl.*, **35**(7), 763-784.
Varol, C.A. (2001), "Increasing the efficiency of wind turbine", *Wind Eng. Ind. Aerod.*, **89**, 809-815.
Yao, J., Wang, W., Yuan, W., Wang, H. and Cao, L. (2012), "Analysis of the influence of turbulence model changes to aerodynamic performance of vertical axis wind turbine", *Procedia Eng*., **31**, 274-281.
Wilcox, D. (1998), *Turbulence modeling for CFD, California:* DCW Industries, Inc., La Canada.

CC